Generalized IDA-PBC Control Using Enhanced Decoupled Power Sharing for Parallel Distributed Generators in Standalone Microgrids

Nidhal Khefifi, Azeddine Houari, Mohamed Machmoum, Abdelhakim Saim, Malek Ghanes

Generalized IDA-PBC Control Using Enhanced Decoupled Power Sharing for Parallel Distributed Generators in Standalone Microgrids

Nidhal Khefifi, Azeddine Houari, Mohamed Machmoum, Abdelhakim Saim, and Malek Ghanes

***Abstract*— The development of an advanced modular control strategy for distributed generation-based islanded MicroGrids (MGs) is proposed in this article. This control strategy aims at achieving robust performances and accurate load power sharing in spite of system architecture. This strategy is based on the interconnection and damping assignment passivity-based control (IDA-PBC), which provides sufficient conditions to ensure the system modularity and stability. The design methodology of the proposed method is declined into three important steps. The whole system is modeled using the port-controlled Hamiltonian (PCH) formalism, the Hamiltonian function is minimized to synthesize the corresponding control laws, and finally, the stability of the synthesized control laws is verified. In this work, the Hamiltonian function is augmented with an enhanced decoupled droop (E2D) control in order to guarantee the stability of the whole system and ensure accurate power sharing when multiple DG units are interconnected. The effectiveness and modularity of the proposed modular IDA-PBC control with the E2D technique are evaluated and compared with a recent control strategy using an inner proportional-integral control with a decoupled droop technique. Experimental results and discussions are provided under resistive–inductive and nonlinear loading conditions.**

***Index Terms*— Decoupled droop control, distributed generation, load power sharing, microgrid, passivity-based control, port-controlled Hamiltonian (PCH).**

NOMENCLATURE

MG	MicroGrid.
IDA-PBC	Interconnection and damping assignment passivity-based control.
DG	Distributed generator.
PCH	Port-controlled Hamiltonian.
PCC	Point of common coupling.
E2D	Enhanced decoupled droop control.
Ng	Number of DGs.

C_{fi}, L_{fi} and R_{fi}	Filter inductance, capacitance, and equivalent resistance of the DG i,
L_{L_i}	Inductive impedance "i" of the connecting filters to the PCC.
i_{ai}, i_{bi}, i_{ci}	*abc*-inverter-side currents of DG "i."
v_{ai}, v_{bi}, v_{ci}	*abc*-inverter-side output voltages of DG "i."
i_{di}, i_{qi}	*dq*-components of the DG "i" inverter-side currents (i_{ai}, i_{bi}, and i_{ci}).
$v_{di}v_{qi}$	*dq*-components of the DG "i" inverter-side output voltages (v_{ai}, v_{bi}, and v_{ci}).
i_{Ldi}, i_{Lqi}	*dq*-components of the output current of DG"*i.*"
ω_i	Angular frequency of DG "*i.*"
v_{Cai}, $v_{Cbi}v_{Cci}$	*abc*-filter capacitor voltages.
v_{Cdi}, v_{Cqi}	*dq*-components of the *abc*-voltages across capacitor filter C_{fi}.
P_i and Q_i	Measured active and reactive powers at the output of DG "*i.*"
P_i^* and Q_i^*	Reference active and reactive powers at the output of DG "i."
E^* and ω^*	Desired nominal voltage and angular frequency.
$\Delta\omega_{\max}$ and $\Delta E_{\max}$	Maximum angular frequency and voltage. amplitude variations.
ΔP and ΔQ	Active and reactive power deviations.
K_{pi} and K_{qi}	Frequency and voltage droop gains.
Z_{vi}	Virtual impedance "*i.*"
R_{vi} and L_{vi}	Resistive and inductive components of the virtual impedance Z_{vi}.
λ_i and ξ_i	Reactive and active coefficients of the decoupled droop.
τ_{pi} and τ_{qi}	Time constant of the imitated inertia.
S	Laplace operator.
X	State variables vector
U	Control inputs vector.
H	Hamiltonian function.
d	External perturbation.
$\mathcal{J}$ and $\mathcal{R}$	Interconnection and damping matrices.
g	Output matrix.

Manuscript received April 8, 2020; revised September 16, 2020; accepted October 12, 2020. Date of publication October 28, 2020; date of current version July 30, 2021. This work was supported by the IREENA RFI WISE Fund. Recommended for publication by Associate Editor Dehong M. Xu. *(Corresponding author: Nidhal Khefifi.)*

Nidhal Khefifi, Azeddine Houari, Mohamed Machmoum, and Abdelhakim Saim are with the Institut de Recherche en Energie Electrique de Nantes Atlantique, University of Nantes, 44602 Saint-Nazaire, France (e-mail: nidhal.khefifi@etu.univ-nantes.fr; azeddine.houari@univ-nantes.fr; machmoum@univ-nantes.fr; abdelhakim.saim@univ-nantes.fr).

Malek Ghanes is with the École Centrale de Nantes-LS2N, UMR CNRS 6004, 44321 Nantes, France (e-mail: malek.ghanes@ec-nantes.fr).

Color versions of one or more of the figures in this article are available online at https://ieeexplore.ieee.org.

Digital Object Identifier 10.1109/JESTPE.2020.3034464

n and m	Number of state and inputs variables for a single generator.
x_i	DG "i" state variables vector.
u_i	DG "i" control inputs vector.
H_i	DG "i" energy.
g_i	DG "i" input matrix.
$\mathcal{J}_i$ and $\mathcal{R}_i$	DG "i" interconnection and damping matrices.
d_i	DG "i" external perturbations.
H_{di}	DG "i" desired energy function.
$\mathcal{J}_{di}$ and $\mathcal{R}_{di}$	DG "i" desired interconnection and damping matrix.
x_i^*	DG "i" desired state-space vector at the equilibrium point.
J_{ai} and $\mathcal{R}_{ai}$	DG "i" new assigned interconnection and damping matrix.
β_i	DG "i" applied control.
E_i^{ref} and ω_i^{ref}	DG "i" voltage and frequency references.
i_{di}^* and i_{qi}^*	DG "i" current references.
v_{Cdi}^* and v_{Cqi}^*	DG "i" voltage reference.
a_{ij}	Parameters for the IDA-PBC controller.
NL	Nonlinear load.
RL	Resistive–inductive load.
DTS	Decoupled trigonometric saturated droop control.
G_V and G_C	PI transfer functions of the outer and inner loops of the compared controller.
k_{pV} and k_{iV}	Proportional and the integral PI control gains of the voltage loop.
k_{pC} and k_{iC}	Proportional and the integral PI control gains of the current loop.
$\mathrm{Kpf}_{\max}$ and $\mathrm{KIf}_{\max}$	Proportional and the integral coefficient related to the frequency and voltage of virtual power sag limit of the decoupled trigonometric control.
δ_f and δ_E	Coefficients fixing the variation limits of voltage and frequency of the trigonometric function.
μ_p and μ_q	Concavity coefficients of the trigonometric function.

I. Introduction

TODAYS' energy transition challenges make the emergence of MGs with renewable energy resources integration as a key solution to meet with numerous climate, technoeconomic, and energy-resiliency requirements [1]. In order to meet with these requirements, many sustainable energy technologies are exploited, including solar photovoltaic panels, wind turbines, and energy storage systems [2], [3]. This concept integrates multiple distributed generators (DGs) that operate near to the point of power consumption to supply end users either in islanded or in grid-connected operation mode [4]–[7]. In the islanded mode, the electricity requirements are generated close to end users, which offers more flexibility, increases energy efficiency, and improves system reliability by integrating multiple DG units [8]–[10]. The use of decentralized droop control methods is widely adopted to control the active and reactive power sharing in MGs essentially when multiple DG units are interconnected. These techniques allow controlling the power participation of each DG unit by regulating the voltage and the frequency locally without communication. The conventional droop method with (P-f) and $(Q - E)$ is applicable when the system shows predominant inductive impedance, with small R/X ratio as it is the case for high- and medium-voltage systems. However, in case of low-voltage MGs, line impedances are mainly resistive with high R/X ratio or even a complex impedance with equivalent resistive–inductive behavior, which implies that the conventional droop technique is no longer effective in low-voltage MGs [11]. In this situation, the coupling between active and reactive powers is strengthened, which makes their control more difficult, resulting in inaccurate power-sharing and stability problems [12]. To solve these problems and improve power-sharing accuracy, several droop control techniques are proposed in the literature. A power transformation droop technique in which modified active and reactive power expressions are adopted instead of the measured ones [13]. Although this technique shows interesting power sharing performances, it increases control complexity. Alternatively, the use of virtual impedances through the addition of virtual passive elements is widely employed in order to enforce the desired behavior and mitigate the existing coupling between active and reactive powers [14], [15]. Even though the addition of virtual passive elements considerably improves the desired impedance predominance without inflicting additional power losses, the output voltage amplitude can drop considerably. In the same line, an advanced droop control technique with additional decoupling signals and scheduled decoupling gains have been proposed in [16]. This technique allows achieving accurate power sharing, but the addition of supplementary signals can affect the steady-state error. To solve this problem, distributed cooperative control techniques have been proposed in [17]. This technique achieves satisfactory performances, but it requires advanced communications limiting its exploitation. In [18] and [19], a DTS droop controller is proposed achieving stable power sharing and proper dynamic decoupling between active and reactive powers irrespective of lines impedances behavior. However, this technique suffers from relatively high computing time as the control complexity is increased requiring multiple trigonometric operations. All these techniques require considerable knowledge on the MG system architecture and parameters, which cannot be guaranteed when the MG is subject to arbitrary loads and DGs' connection and disconnection. Therefore, when considering scalable MGs, the system and control laws parameters become no longer convenient, and the system stability will not be assured. In other side, and in order to maintain the output voltage amplitude and frequency within acceptable ranges, some research works propose adding a higher control level commonly known as a secondary control.

This communication-based control level provides means to manage the interaction between DG units, restore voltage and frequency values, and ensure in consequence more accurate power sharing while preserving the system stability. Similarly, secondary control techniques have been proposed using either stochastic control [20] or neural network techniques [21], [22]. These controllers have some limitations essentially related to their complex structure and their dependence on high-speed communication. Conversely, the use of decentralized control approaches can be more interesting as they do not require communication. In addition, the use of lower control levels is required to maintain the output voltage of each DG unit within standardized electrical boundaries [23], [24]. At this level, many control techniques can be found in the literature, including classical control techniques [25], [26], nonlinear control techniques [15], [27], learning-based control methods [28], [29], and predictive control techniques [30], [31]. These methods can ensure satisfactory control performances but suffer from their dependence on the system parameters. This model dependence may reduce their effectiveness in the case of scalable MG applications. Indeed, in such applications, the system architecture may evolve, and thus, the control laws no longer guarantee the desired performances and system stability. At this level, the use of energetic approaches, such as the IDA-PBC method, is recommended. This control method can be interesting for MG applications as it can synthesize robust control laws and provide sufficient conditions to guarantee the stability of complex and multiphysical systems despite the existing coupling between them [32], [33]. This method has been particularly used in distributed systems since it allows the synthesis of modular control laws [34].

In this article, the development of an advanced modular control strategy based on the IDA-PBC is proposed. The objectives of the proposed strategy are to ensure the system modularity and stability while achieving robust performances and accurate load power sharing in spite of system architecture. For design purposes, the whole system is first modeled using the PCH formalism before the Hamiltonian function is minimized to synthesize the control laws, and finally, the stability of the synthesized control laws is verified. The Hamiltonian function refers to the system physical energy and is assimilated to the Lyapunov function, which allows guaranteeing the stability of the synthesized controllers. The PCH formalism is characterized by an interesting symplectic geometrical form with a diagonal skew-symmetric matrix that allows synthetizing modular control laws. The resulting control laws guarantee the system modularity and stability even in the case of system reconfiguration and expansion. To further exploit the advantages offered by the Hamiltonian formalism and achieve accurate power sharing when multiple DG units are interconnected, the Hamiltonian function is augmented with an E2D power-sharing controller. The proposed E2D controller uses an additional filter that improves the system response against transients by introducing virtual inertia, while the Hamiltonian form is maintained. This modeling formalism allows guaranteeing a generic control synthesis based on the IDA-PBC method. This technique is applied to design

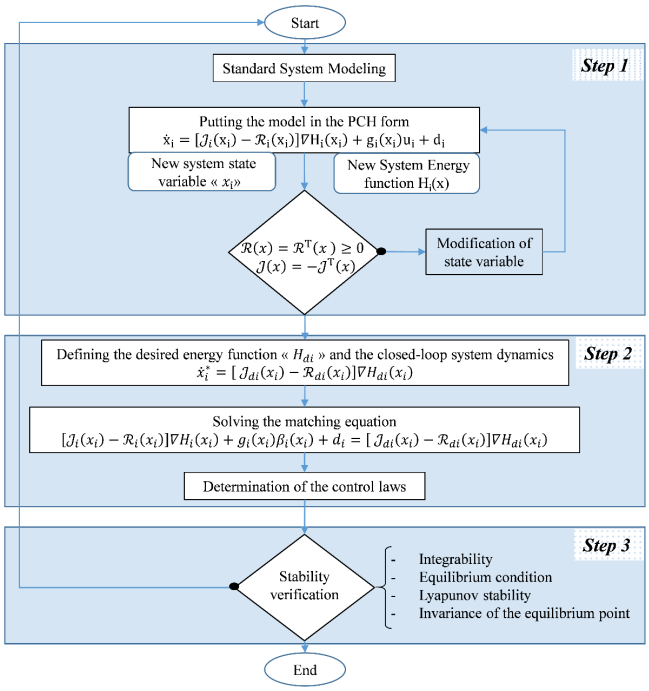

Fig. 1. Steps for IDA-PBC control synthesis.

both voltage and power-sharing controllers with the objective to ensure high-voltage quality and guarantee accurate active and reactive power sharing between interconnected DG units. The effectiveness and modularity of the proposed IDA-PBC control with the E2D technique are evaluated and compared with a recent control strategy proposing the use of an inner proportional–integral control with a saturated trigonometric droop control technique.

This article is organized as follows. A short overview of the IDA-PBC method and its theoretical synthesis is presented in Section II. Section III details the design methodology of the IDA-PBC control for the studied MG system. Section IV introduces a recent decoupled droop control used as a comparative technique method. To demonstrate the effectiveness of the proposed IDA-PBC controller with the E2D control, detailed comparative experimental results are presented in Section V. Finally, this article ends with a conclusion in Section VI.

II. IDA-PBC Methodology

This section presents the essential knowledge and synthesis steps of the control laws to understand the proposed modular IDA-PBC control and the Hamiltonian formalism. The detailed control synthesis steps are presented in Fig. 1 and described as follows.

Step1 (System Modeling on the PCH Form): To synthesize the IDA-PBC controller, the system is first modeled in the PCH form described in expression (1) [34]. The use of this model form is motivated not only by the use of an energy approach necessary to synthesize the desired control but also by its modular structure allowing the modeling of several connected parallel DGs units to the PCC

$$\dot{x} = [\mathcal{J}(x) - \mathcal{R}(x)]\nabla H(x) + g(x)u + d. \tag{1}$$

The modular form of the previous PCH formula is detailed in the following expressions where:

$$x = \begin{bmatrix} x_1 \\ \vdots \\ x_i \\ \vdots \\ x_{ng} \end{bmatrix}; \quad u(x) = \begin{bmatrix} u_1 \\ \vdots \\ u_i \\ \vdots \\ u_{ng} \end{bmatrix}; \quad d = \begin{bmatrix} d_1 \\ \vdots \\ d_i \\ \vdots \\ d_{ng} \end{bmatrix};$$

$$g(x) = \begin{bmatrix} g_1 & \cdots & 0 & \cdots & 0 \\ \vdots & \ddots & \vdots & & \vdots \\ 0 & & g_i & & 0 \\ \vdots & & \vdots & \ddots & \vdots \\ 0 & \cdots & 0 & \cdots & g_{ng} \end{bmatrix}$$

$$\mathcal{J}(x) = \begin{bmatrix} \mathcal{J}_1(x_1) & \cdots & 0 & \cdots & 0 \\ \vdots & \ddots & \vdots & & \vdots \\ 0 & & \mathcal{J}_i(x_i) & & 0 \\ \vdots & & & \ddots & \vdots \\ 0 & \cdots & 0 & \cdots & \mathcal{J}_{ng}(x_{ng}) \end{bmatrix}$$

$$\mathcal{R}(x) = \begin{bmatrix} \mathcal{R}_1(x_1) & \cdots & 0 & \cdots & 0 \\ \vdots & \ddots & \vdots & & \vdots \\ 0 & & \mathcal{R}_i(x_i) & & 0 \\ \vdots & & & \ddots & \vdots \\ 0 & \cdots & 0 & \cdots & \mathcal{R}_{ng}(x_{ng}) \end{bmatrix}$$

$$H(x) = \begin{bmatrix} H_1 & \cdots & 0 & \cdots & 0 \\ \vdots & \ddots & \vdots & & \vdots \\ 0 & & H_i & & 0 \\ \vdots & & \vdots & \ddots & \vdots \\ 0 & \cdots & 0 & \cdots & H_{ng} \end{bmatrix};$$

$$\text{where } H_i = \frac{1}{2} x_i^{\mathrm{T}} Q_i^{-1} x_i. \tag{2}$$

In these expressions, $x \in \mathcal{R}^{ng}$ is the state vector. $u \in \mathcal{R}^{ng}$ is the control input vector, where "ng" represents the number of parallel DG units. $g(x) \in \mathcal{R}^{ng}$ is the input matrix. $H(x) \in \mathcal{R}^{ng \times ng}$ is a function defining the system energy. "d" is a vector corresponding to the external perturbation. $\mathcal{J}(x) \in \mathcal{R}^{ng \times ng}$ and $\mathcal{R}(x) \in \mathcal{R}^{ng \times ng}$ are, respectively, the interconnection and damping matrices. These two matrices verify $\mathcal{R}(x) = \mathcal{R}^{\mathrm{T}}(x) \geq 0$ and $\mathcal{J}(x) = -\mathcal{J}^{\mathrm{T}}(x)$.

This modular formulation allows the synthesis of a global control for all systems based on only one elementary DG indexed by "i." Following the previous model expression in (1), the elementary model of each DG can be expressed by the following expression:

$$\dot{x}_i = [\mathcal{J}_i(x_i) - \mathcal{R}_i(x_i)] \nabla H_i(x_i) + g_i(x_i) u_i + d_i. \tag{3}$$

In this model, $x_i \in \mathcal{R}^n$ represents the state vector and $u_i \in \mathcal{R}^m$ depicts the input control vector in which "n" and "m" represent, respectively, the number of states and inputs variables for a single generator and guarantee $m < n$. $H_i(x_i)$ is the energy of the elementary DG_i system, $g_i(x_i)$ is the input matrix of the elementary DG_i system, and d_i is a vector that describes the external perturbations. $\mathcal{R}_i(x_i)$ and $\mathcal{J}_i(x_i)$ are, respectively, the damping and interconnection matrices that verify $\mathcal{R}_i(x_i) = \mathcal{R}_i^{\mathrm{T}}(x_i) \geq 0$ and $\mathcal{J}_i(x_i) = -\mathcal{J}_i^{\mathrm{T}}(x_i)$.

Step 2 (IDA PBC Law Design): In order to synthesize the IDA-PBC controller consisting to shape the energy of the system by controlling its dissipation, the steps presented in Fig. 1 are to follow.

First of all, designers need to identify the desired energy function of the studied system noted generally by $H_{di}(x_i)$. Then, the control "u" is set to assure not only the PCH form but also the desired dynamic performances expressed in the following equation:

$$\dot{x}_i^* = [\mathcal{J}_{di}(x_i) - \mathcal{R}_{di}(x_i)] \nabla H_{di}(x_i). \tag{4}$$

Expression (4) describes the desired state-space representation equations at the equilibrium point x_i^* in the port Hamiltonian formulation, where $H_{di}(x_i)$ is the energy function that characterizes the local minimum at the desired equilibrium point. $\mathcal{J}_{di}$ and $\mathcal{R}_{di}$ represent, respectively, the desired interconnection and damping matrix. These matrices satisfy, respectively: $\mathcal{J}_{di}(x_i) = -\mathcal{J}_{di}^{\mathrm{T}}(x_i)$ and $\mathcal{R}_{di}(x_i) = \mathcal{R}_{di}^{\mathrm{T}}(x_i) \geq 0$.

The calculation of the control laws is done by solving the matching equation defined by (5). This equation links the expression of the closed loop (4) to that of the open loop (3)

$$[\mathcal{J}_i(x_i) - \mathcal{R}_i(x_i)] \nabla H_i(x_i) + g_i(x_i) \beta_i(x_i) + d_i = [\mathcal{J}_{di}(x_i) - \mathcal{R}_{di}(x_i)] \nabla H_{di}(x_i). \tag{5}$$

Solving the matching equation (5) requires the use of new assigned matrices $J_{ai}(x_i)$ and $R_{ai}(x_i)$ and a new vector called $K_i(x_i)$ [35]. These components are fixed by the designer to facilitate the synthesis of the applied control defined by $u_i = \beta_i(x_i)$.

This matching equation can be expressed differently by the following equation:

$$[(\mathcal{J}_i(x_i) + \mathcal{J}_{ai}(x_i)) - (\mathcal{R}_i(x_i) + \mathcal{R}_{ai}(x_i)] K_i(x_i) = -[\mathcal{J}_{ai}(x_i) - \mathcal{R}_{ai}(x_i)] \nabla H_i(x_i) + g_i(x_i) \beta_i(x_i) + d_i. \tag{6}$$

The determination of the elements that constitute the matrices $\mathcal{R}_{ai}(x_i)$ and $\mathcal{J}_{ai}(x_i)$ depends on the control objectives. The designer is free in his choice. Often, in electrical power systems, the interconnection matrix is set to avoid the coupling between voltage and current where the damping matrix is selected to enhance the dynamic convergence.

Step 3 (Stability Verification): This last step is mandatory in order to prove the stability of the system around its equilibrium point x_i^*. In this phase, the designer must verify that the resulting closed-loop system keeps the PCH form and shows the desired dynamics described in (4). Therefore, the selected damping and interconnection matrix $R_{ai}(x_i)$ and $J_{ai}(x_i)$ need to fulfill the following five conditions [36].

1) *Structure Preservation:* $\mathcal{R}_{di}(x_i) = \mathcal{R}_i(x_i) + \mathcal{R}_{ai}(x_i) = \mathcal{R}_{di}^{\mathrm{T}}(x_i) \geq 0$ and $\mathcal{J}_{di}(x_i) = \mathcal{J}_i(x_i) + \mathcal{J}_{ai}(x_i) = -\mathcal{J}_{di}^{\mathrm{T}}(x_i)$.
2) *Integrability:* $K_i(x_i)$ is the gradient of a scalar function: $\nabla K_i(x_i) = [\nabla K_i(x_i)]^{\mathrm{T}}$.
3) *Equilibrium Condition:* $K_i(x_i)$ at x_i^* satisfies: $K_i(x_i^*) = -\nabla H_i(x_i^*)$.

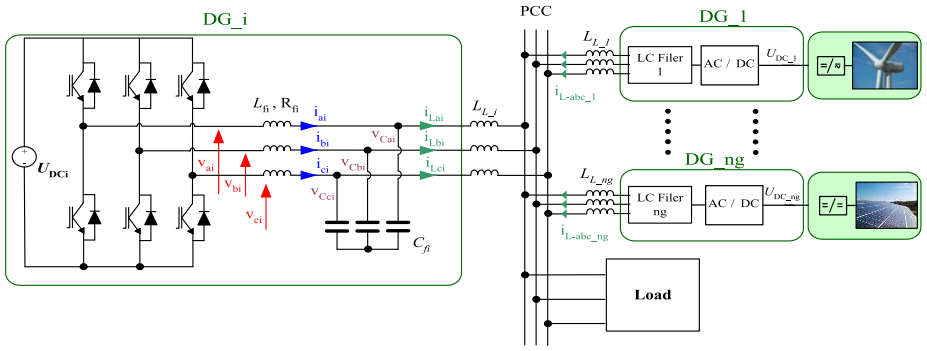

Fig. 2. Structure of the studied system.

4) *Lyapunov Stability*: The Jacobian of $K_i(x_i)$ at x_i^* satisfies the bound: $\nabla K_i(x_i^*) > -\nabla^2 H_i(x_i^*)$.
5) *Invariance of the Equilibrium Point [37]*: $-[\nabla H_{di}]^{\mathrm{T}} \mathcal{R}_{di}(x_i^*) \nabla H_{di} \leq 0$.

Condition 5) guarantees that the solution is bounded for the desired function H_{di}.

Checking the five previous conditions proves that the control of the closed-loop system $u_i = \beta_i(x_i)$ will be a port-controlled where $K_i(x_i) = \nabla H_{ai}(x_i)$ and $H_{di}(x_i) = H_i(x_i) + H_{ai}(x_i)$.

III. Application of the IDA-PBC to the Studied MG

This section presents the application of the proposed method to the studied MG by considering the design steps that have already been presented in Fig. 1.

A. Step1: System Modeling on the PCH Form

The studied islanded MG is shown in Fig. 2. It is composed of "ng" parallel three-phase inverters that supply a local load connected to the (PCC) via *LCL* filter. The local load is supplied by power provided from primary sources. In this work, the primary sources are supposed constant and are presented by a dc link. In this scheme, R_{fi}, C_{fi}, and L_{fi} represent, respectively, the internal per-phase resistance, capacitor, and inductance of the inverter output filter. The link between DGs and the PCC is modeled by an impedance characterized by an inductance L_{L_i}.

In each DG unit, a low-level control is implemented to regulate at the same time the output voltage across the capacitors C_{fi} and the power sharing using a droop control technique. This level guarantees load power sharing between the paralleled DGs units. To obtain the individual control laws, each DG system is separately modeled by an internal and an interaction model.

1) Internal Model: The internal model of each DG unit that corresponds to the inverter output *LC* filter is described in the rotating *dq* reference by the following equations:

$$\begin{aligned} L_{fi}\frac{di_{di}}{dt} &= -R_{fi}i_{di} + L_{fi}\omega_i i_{qi} + v_{di} - v_{Cdi} \\ L_{fi}\frac{di_{qi}}{dt} &= -R_{fi}i_{qi} - L_{fi}\omega_i i_{di} + v_{qi} - v_{Cqi} \\ C_{fi}\frac{dv_{Cdi}}{dt} &= i_{di} - i_{Ldi} + C_{fi}\omega_i v_{Cqi} \end{aligned}$$

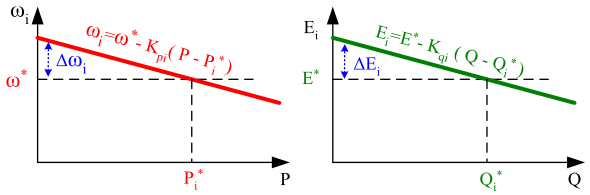

Fig. 3. Classical droop control for MG with inductive behavior.

$$C_{fi}\frac{dv_{Cqi}}{dt} = i_{qi} - i_{Lqi} - C_{fi}\omega_i v_{Cdi}. \tag{7}$$

In these expressions, "i" designates the index of each DG. v_{di} and v_{qi} and i_{Ldi} and i_{Lqi} represent, respectively, the output voltages of the inverter "i" and the load currents in each DG unit in the *dq*-frame reference. i_{di} and i_{qi} and v_{Cdi} and v_{Cqi} represent separately the *dq*-components of the line currents (i_{ai}, i_{bi}, and i_{ci}) and the voltage through the capacitors C_{fi}. Finally, ω_i denotes the angular frequency in DG_i.

2) Interaction Model: The modeling of parallel DG units needs to take into consideration the interaction between them to avoid the problem of circulating currents [38]. This interaction is modeled by droop equations. In fact, systems based on renewable energies have low inertia. The idea of using the droop equations consists of conferring to the system a kind of virtual inertia so that it behaves like a conventional generator in front of disturbances [39]. The use of these equations permits to ensure the power sharing without the need for expensive communications protocol [9]. A brief review of the traditional droop control is presented in this section. In fact, in most low-voltage DG systems, distances between DGs are modeled by inductors, which promotes the inductive behavior of the system. In this case, the use of the classical droop control, presented in (8), is justified. It permits as presented in Fig. 3 to control the active power by acting on the frequency component and controlling the reactive one by managing the voltage amplitude [38]

$$\begin{aligned} \dot{\delta}_i &= \omega_i \\ \omega_i &= \omega^* - K_{pi}(P_i - P_i^*) \\ E_i &= E^* - K_{qi}(Q_i - Q_i^*) \end{aligned} \tag{8}$$

where P_i and Q_i are, respectively, the measured active and reactive power at the filter output , P_i^* and Q_i^* denote,

respectively, the desired active and reactive power references of DG$_i$, $\omega^* \in R$ is the desired nominal frequency, and E^* is the desired nominal voltage amplitude. Finally, frequency and voltage droop gains are designed, respectively, by K_{pi} and K_{qi}.

These coefficients are defined by the following equations:

$$K_{pi} = \frac{\Delta\omega_{\max}}{\Delta P}$$
$$K_{qi} = \frac{\Delta E_{\max}}{\Delta Q}. \tag{9}$$

In this equation, $\Delta\omega_{\max}$ is the maximum tolerable pulsation deviation related to the active power variation ΔP. In the same way, $\Delta E_{\max}$ is the maximum authorized voltage variation associated with the reactive power change ΔQ.

In practice, it is difficult to know the impedance value connecting each DG unit to the PCC. Under such conditions, the conventional droop alone cannot achieve the desired reactive and active power sharing. The interest in adding a virtual impedance to the primary control structure allows first to support the inductive behavior of the output impedance and second to avoid the additional cost of installing real physical impedances [4].

The added virtual impedance control law expression for each (DG) is described in the following equation [40]:

$$L_{vi}\frac{di_{Ldi}}{dt} = v_{Cdi} - Z_{vi}i_{Ldi}$$
$$L_{vi}\frac{di_{Lqi}}{dt} = v_{Cqi} - Z_{vi}i_{Lqi} \tag{10}$$

where $Z_{vi} = R_{vi} + L_{vi}\omega_i$, with R_{vi} and L_{vi}, respectively, the value of resistance and inductance of the used virtual impedances.

Note that in case, in the case of low-voltage systems, the frequency variation influences widely both the active and reactive power and, consequently, the voltage amplitudes. Moreover, the value of the virtual impedance is limited by the droop voltage and system stability. This means that the coupling cannot be effectively eliminated. To guarantee the decoupling between the reactive and the active power, decoupling control terms are introduced to the classical droop to ensure the compensation of the voltage and frequency deviations. The expression of the previous classical droop control (8) becomes as follows:

$$\dot{\delta}_i = \omega_i$$
$$\omega_i = \omega^* - K_{pi}\left(P_i - P_i^*\right) + \lambda_i(E^* - E_i)$$
$$E_i = E^* - K_{qi}\left(Q_i - Q_i^*\right) + \xi_i(\omega^* - \omega_i) \tag{11}$$

where λ_i and ξ_i present, respectively, the decoupling reactive and active droop coefficients.

The studied system is based on renewable energy systems. These systems are characterized by weak inertia. To improve the behavior of these systems in front of current disturbances and to achieve high-voltage and frequency regulation, additional virtual inertia is introduced to expressions (11). This additional inertia, modeled by a low-pass filter, improves the stability of each DG system.

The new formula of the E2D control is written as follows:

$$\frac{d\delta_i}{dt} = \omega_i$$
$$\tau_{pi}\frac{d\omega_i}{dt} = K_{pi}\left(P_i^* - P_i\right) + \lambda_i\left(E_i^* - E_i\right) + (\omega_i - \omega_i^*)$$
$$\tau_{qi}\frac{dE_i}{dt} = K_{qi}\left(Q_i^* - Q_i\right) + \xi_i(\omega_i^* - \omega_i) + (E_i - E_i^*) \tag{12}$$

where τ_{pi} and τ_{qi} correspond to the time constant of the low-pass filter used to mimic the inertia of the real synchronous generator.

In regard to the planned control that contains the local and the interconnected model composed by the enhanced droop control, the virtual impedance, and the individual DGi model, the candidate Hamiltonian function can be taken as the sum of all the energy stored in the used filters

$$H_i(x_i) = \frac{1}{2}L_{fi}i_{di}^2 + \frac{1}{2}L_{fi}i_{qi}^2 + \frac{1}{2}C_{fi}v_{Cdi}^2 + \frac{1}{2}C_{fi}v_{Cqi}^2 + \frac{1}{2}\tau_{pi}\omega_i^2 + \frac{1}{2}\tau_{qi}E_i^2 + \frac{1}{2}L_{vi}i_{Ldi}^2 + \frac{1}{2}L_{vi}i_{Lqi}^2. \tag{13}$$

For the proposed energy function, the chosen state variable vector is designed as

$$x_i = \begin{bmatrix} x_{1i} & x_{2i} & x_{3i} & x_{4i} & x_{5i} & x_{6i} & x_{7i} & x_{8i} \end{bmatrix}^{\mathrm{T}} = Q_i\begin{bmatrix} i_{di} & i_{qi} & v_{Cdi} & v_{Cqi} & i_{di} & i_{qi} & i_{di} & i_{qi} \end{bmatrix}^{\mathrm{T}}$$

where $Q_i = \mathrm{diag}\{L_{fi}\ L_{fi}\ C_{fi}\ C_{fi}\ \tau_{pi}\ \tau_{qi}\ L_{vi}\ L_{vi}\}$ and $H_i(x) = (1/2)x_i^{\mathrm{T}}Q_i^{-1}x_i$.

Using (8), (10), and (12), the modular system modeling in the PCH form of a DGi system is derived as follows considering $\nabla H_i(x_i) = [i_{di}\ i_{qi}\ v_{Cdi}\ v_{Cqi}\ \omega_i\ E_i\ i_{Ldi}\ i_{Lqi}]^{\mathrm{T}}$.

In this model, we consider that $\lambda_i = -\xi_i$

$$\mathcal{J}_i(x_i) = \begin{bmatrix} 0 & L_{fi}\omega_i & -1 & 0 & 0 & 0 & 0 & 0 \\ -L_{fi}\omega_i & 0 & 0 & -1 & 0 & 0 & 0 & 0 \\ 1 & 0 & 0 & C_{fi}\omega_i & 0 & 0 & -1 & 0 \\ 0 & 1 & -C_{fi}\omega_i & 0 & 0 & 0 & 0 & -1 \\ 0 & 0 & 0 & 0 & 0 & -\lambda_i & 0 & 0 \\ 0 & 0 & 0 & 0 & -\xi_i & 0 & 0 & 0 \\ 0 & 0 & 1 & 0 & 0 & 0 & 0 & 0 \\ 0 & 0 & 0 & 1 & 0 & 0 & 0 & 0 \end{bmatrix};$$

$$d_i = \begin{bmatrix} 0 \\ 0 \\ 0 \\ 0 \\ \omega^* + K_{pi}P_i^* + \lambda_i E_i^* \\ E^* + K_{qi}Q_i^* + \xi_i\omega_i^* \\ 0 \\ 0 \end{bmatrix}$$

$$\mathcal{R}_i(x_i) = \begin{bmatrix} R_{fi} & 0 & 0 & 0 & 0 & 0 & 0 & 0 \\ 0 & R_{fi} & 0 & 0 & 0 & 0 & 0 & 0 \\ 0 & 0 & 0 & 0 & 0 & 0 & 0 & 0 \\ 0 & 0 & 0 & 0 & 0 & 0 & 0 & 0 \\ 0 & 0 & 0 & 0 & 1 & 0 & 0 & 0 \\ 0 & 0 & 0 & 0 & 0 & 1 & 0 & 0 \\ 0 & 0 & 0 & 0 & 0 & 0 & Z_v & 0 \\ 0 & 0 & 0 & 0 & 0 & 0 & 0 & Z_v \end{bmatrix};$$

$$g_i(x_i) = \begin{bmatrix} 1 & 0 & 0 & 0 \\ 0 & 1 & 0 & 0 \\ 0 & 0 & 0 & 0 \\ 0 & 0 & 0 & 0 \\ 0 & 0 & -K_{pi} & 0 \\ 0 & 0 & 0 & -K_{qi} \\ 0 & 0 & 0 & 0 \\ 0 & 0 & 0 & 0 \end{bmatrix}; u_i = \begin{bmatrix} v_{di} \\ v_{qi} \\ P_i \\ Q_i \end{bmatrix} \tag{14}$$

$$\begin{aligned} H_{di}(x_i^*) &= \frac{1}{2}L_{fi}\left(i_{di}-i_{di}^*\right)^2 + \frac{1}{2}L_{fi}\left(i_{qi}-i_{qi}^*\right)^2 \\ &+\frac{1}{2}C_{fi}\left(v_{Cdi}-v_{Cdi}^*\right)^2 + \frac{1}{2}C_{fi}\left(v_{Cqi}-v_{Cqi}^*\right)^2 \\ &+\frac{1}{2}\tau_{pi}\left(\omega_i-\omega_i^*\right)^2 + \frac{1}{2}\tau_{qi}\left(E_i-E_i^*\right)^2 \\ &+\frac{1}{2}L_{vi}\left(i_{Ldi}-i_{Ldi}^*\right)^2 + \frac{1}{2}L_{vi}\left(i_{Lqi}-i_{Lqi}^*\right)^2 \\ &= \frac{1}{2L_{fi}}\left(x_{1i}-x_{1i}^*\right)^2 + \frac{1}{2L_{fi}}\left(x_{2i}-x_{2i}^*\right)^2 \\ &+\frac{1}{2C_{fi}}\left(x_{3i}-x_{3i}^*\right)^2 + \frac{1}{2C_{fi}}\left(x_{4i}-x_{4i}^*\right)^2 \\ &+\frac{1}{2\tau_{pi}}\left(x_{5i}-x_{5i}^*\right)^2 + \frac{1}{2\tau_{qi}}\left(x_{6i}-x_{6i}^*\right)^2 \\ &+\frac{1}{2L_{vi}}\left(x_{7i}-x_{7i}^*\right)^2 + \frac{1}{2L_{vi}}\left(x_{8i}-x_{8i}^*\right)^2. \end{aligned} \tag{15}$$

B. Step2: IDA PBC Laws Design

This section is dedicated to the synthesis of the proposed control illustrated in the synoptic scheme presented in Fig. 4.

The desired Hamiltonian function has a local minimum at the desired equilibrium point x_i^*, which is defined as presented in (15).

In these expressions, the designer considers the open-loop Hamiltonian function defined in (3) and the desired control objective (4) that allows the system to reach minimal energy at the desired equilibrium point x_i^*. Then, with regard to the initial form of the interconnection and damping matrices ($\mathcal{J}_i(x_i)$ and $\mathcal{R}_i(x_i)$) presented in (14), the new desired matrices can be expressed as

$$\mathcal{J}_{di}(x_i) = \begin{bmatrix} 0 & 0 & a_{13i} & 0 & 0 & 0 & 0 & 0 \\ 0 & 0 & 0 & a_{24i} & 0 & 0 & 0 & 0 \\ a_{31i} & 0 & 0 & 0 & 0 & 0 & a_{37i} & 0 \\ 0 & a_{42i} & 0 & 0 & 0 & 0 & 0 & a_{48i} \\ 0 & 0 & 0 & 0 & 0 & 0 & 0 & 0 \\ 0 & 0 & 0 & 0 & 0 & 0 & 0 & 0 \\ 0 & 0 & a_{73i} & 0 & 0 & 0 & 0 & 0 \\ 0 & 0 & 0 & a_{84i} & 0 & 0 & 0 & 0 \end{bmatrix}$$

$$\mathcal{R}_{di}(x_i) = \begin{bmatrix} a_{11i} & 0 & 0 & 0 & 0 & 0 & 0 & 0 \\ 0 & a_{22i} & 0 & 0 & 0 & 0 & 0 & 0 \\ 0 & 0 & a_{33i} & 0 & 0 & 0 & 0 & 0 \\ 0 & 0 & 0 & a_{44i} & 0 & 0 & 0 & 0 \\ 0 & 0 & 0 & 0 & a_{55i} & 0 & 0 & 0 \\ 0 & 0 & 0 & 0 & 0 & a_{66i} & 0 & 0 \\ 0 & 0 & 0 & 0 & 0 & 0 & a_{77i} & 0 \\ 0 & 0 & 0 & 0 & 0 & 0 & 0 & a_{88i} \end{bmatrix} \tag{16}$$

where $a_{ij} = -a_{ji}$ and $a_{ii} \geq 0$ with $i, j = \{1, \ldots, 8\}$ for $i \neq j$.

$\mathcal{R}_{di}(x_i) = R_{di}^{\mathrm{T}}(x_i) \geq 0$ and $\mathcal{J}_{di}(x_i) = -\mathcal{J}_{di}^{\mathrm{T}}(x_i)$ are, respectively, the desired damping and interconnection matrices certifying $a_{13i} = -a_{31i} = -1$,$a_{24i} = -a_{42i} = -1$,$a_{73i} = -a_{37i} = -1$, $a_{84i} = -a_{48i} = -1$, and $a_{jji} \geq 0$, where $j = \{1, \ldots, 8\}$ and $a_{55i} = a_{66i} = 0$.

The implemented control laws are obtained by solving the matching equation (5) and are based on the four following control loops.

1) Enhanced Decoupled Droop Control Loop: This loop is used to generate automatically the reference voltage (E_i^{ref} and ω_i^{ref}) according to the measured powers

$$\begin{aligned} \omega_i^{\mathrm{ref}} &= \omega^* - K_{pi}\left(P_i - P_i^*\right) + \lambda_i\left(E_i^* - E_i\right) + a_{55i}(\omega_i - \omega^*) \\ E_i^{\mathrm{ref}} &= E^* - K_{qi}\left(Q_i - Q_i^*\right) + \xi_i\left(\omega_i^* - \omega_i\right) + a_{66i}\left(E_i - E^*\right). \end{aligned} \tag{17}$$

Both of the reference voltage amplitudes and the reference pulsations of the E2D control are composed of the classical droop control, the decoupling active and reactive power expressions and an additional compensation term for the used references.

E_i^{ref} and ω_i^{ref} are used to provide the three voltage references for each DG system in the following equation:

$$\begin{aligned} V_{1\mathrm{ref}(i)}(t) &= E_i^{\mathrm{ref}} \sin \in (\omega_i^{\mathrm{ref}}(t)) \\ V_{2\mathrm{ref}(i)} &= E_i^{\mathrm{ref}} \sin\left(\omega_i^{\mathrm{ref}}(t) - \frac{2\pi}{3}\right) \\ V_{3\mathrm{ref}(i)} &= E_i^{\mathrm{ref}} \sin\left(\omega_i^{\mathrm{ref}}(t) + \frac{2\pi}{3}\right). \end{aligned} \tag{18}$$

These voltage references will be expressed in a stationary framework to obtain the *dq*-axis voltage references defined by V_{cdi}^* and V_{cqi}^*.

2) Virtual Impedance Loop: Improving the system response and the power sharing needs to take into consideration the output impedance. At this stage of control, a virtual impedance is enforced as follows:

$$\begin{aligned} v_{Cdi-Zv}^* &= (R_{vi} + L_{vi}\omega_i)i_{Ldi} + a_{77i}(i_{Ldi} - i_{Ldi}^*) \\ v_{Cqi-Zv}^* &= (R_{vi} + L_{vi}\omega_i)i_{Lqi} + a_{88i}(i_{Lqi} - i_{Lqi}^*). \end{aligned} \tag{19}$$

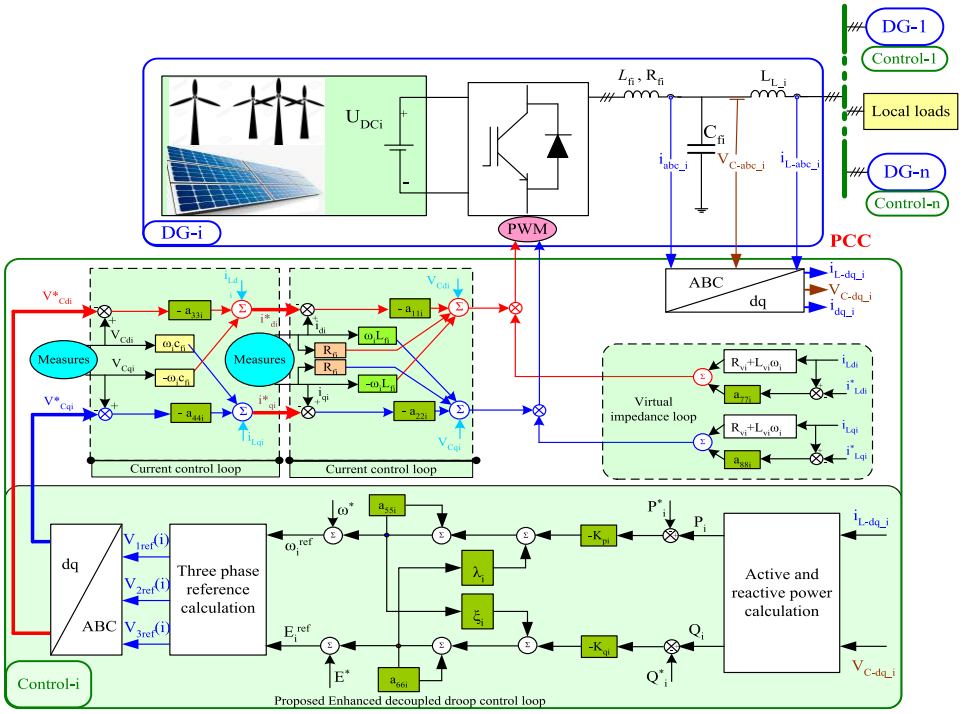

Fig. 4. Structure of the used global control.

3) Voltage Loop Control: The third loop is the voltage loop control; it is used to generate the *dq*-currents reference to the currents loop

$$\begin{aligned} v^*_{Cdi-Zv} &= (R_{vi} + L_{vi}\omega_i)i_{Ldi} + a_{77i}(i_{Ldi} - i^*_{Ldi}) \\ v^*_{Cqi-Zv} &= (R_{vi} + L_{vi}\omega_i)i_{Lqi} + a_{88i}(i_{Lqi} - i^*_{Lqi}). \end{aligned} \quad (20)$$

4) Current Loop Control: The inner loop that controls the currents to generate the voltage PWM references of the inverter

$$\begin{aligned} v^*_{Cdi} &= -a_{11i}\left(i_{di} - i^*_{di}\right) + v_{di} - R_{fi}i_{di} + L_{fi}\omega i_{qi} \\ v^*_{Cqi} &= -a_{22i}\left(i_{qi} - i^*_{qi}\right) + v_{qi} - R_{fi}i_{qi} - L_{fi}\omega i_{di}. \end{aligned} \quad (21)$$

C. Step 3: Stability Verification

This section presents the verification of the necessary conditions to guarantee the local stability at the point of equilibrium x^* by applying the proposed controller based on the passivity. The five conditions already presented in Section II are checked.

1) Structure Preservation:

$$\mathcal{J}_{di}(x_i) = \begin{bmatrix} 0 & 0 & a_{13i} & 0 & 0 & 0 & 0 & 0 \\ 0 & 0 & 0 & a_{24i} & 0 & 0 & 0 & 0 \\ a_{31i} & 0 & 0 & 0 & 0 & 0 & a_{37i} & 0 \\ 0 & a_{42i} & 0 & 0 & 0 & 0 & 0 & a_{48i} \\ 0 & 0 & 0 & 0 & 0 & 0 & 0 & 0 \\ 0 & 0 & 0 & 0 & 0 & 0 & 0 & 0 \\ 0 & 0 & a_{73i} & 0 & 0 & 0 & 0 & 0 \\ 0 & 0 & 0 & a_{84i} & 0 & 0 & 0 & 0 \end{bmatrix} = -[\mathcal{J}_{di}(x_i)]^{\mathrm{T}} \quad (22)$$

$$\mathcal{R}_{di}(x_i) = \begin{bmatrix} a_{11i} & 0 & 0 & 0 & 0 & 0 & 0 & 0 \\ 0 & a_{22i} & 0 & 0 & 0 & 0 & 0 & 0 \\ 0 & 0 & a_{33i} & 0 & 0 & 0 & 0 & 0 \\ 0 & 0 & 0 & a_{44i} & 0 & 0 & 0 & 0 \\ 0 & 0 & 0 & 0 & a_{55i} & 0 & 0 & 0 \\ 0 & 0 & 0 & 0 & 0 & a_{66i} & 0 & 0 \\ 0 & 0 & 0 & 0 & 0 & 0 & a_{77i} & 0 \\ 0 & 0 & 0 & 0 & 0 & 0 & 0 & a_{88i} \end{bmatrix} = [\mathcal{R}_{di}(x_i)]^{\mathrm{T}} > 0 \quad (23)$$

where $a_{13i} = -a_{31i}, a_{24i} = -a_{42i}, a_{37i} = -a_{73i}, a_{48i} = -a_{84i}$, and $a_{ppi} \geq 0$ $etk_I > 0$, given that $p = \{1, \ldots, 8\}$.

This proves that the first structural condition 1 is verified.

a) Integrability:

$$\begin{aligned} H_{ai}\left(x^*_i\right) &= H_{di}\left(x^*_i\right) - H_i(x_i) \\ &= \left[\frac{1}{2L_{fi}}\left(x_{1i} - x^*_{1i}\right)^2 + \frac{1}{2L_{fi}}\left(x_{2i} - x^*_{2i}\right)^2 \right. \\ &\quad + \frac{1}{2C_{fi}}\left(x_{3i} - x^*_{3i}\right)^2 + \frac{1}{2C_{fi}}\left(x_{4i} - x^*_{4i}\right)^2 \\ &\quad + \frac{1}{2\tau_{pi}}\left(x_{5i} - x^*_{5i}\right)^2 + \frac{1}{2\tau_{qi}}\left(x_{6i} - x^*_{6i}\right)^2 \\ &\quad \left. + \frac{1}{2L_{vi}}\left(x_{7i} - x^*_{7i}\right)^2 + \frac{1}{2L_{vi}}\left(x_{8i} - x^*_{8i}\right)^2\right] \\ &\quad - \left[\frac{1}{2}\frac{x^2_{1i}}{L_{fi}} + \frac{1}{2}\frac{x^2_{2i}}{L_{fi}}\right. \\ &\quad + \frac{1}{2}\frac{x^2_{3i}}{C_{fi}} + \frac{1}{2}\frac{x^2_{4i}}{C_{fi}} + \frac{1}{2}\frac{x^2_{5i}}{\tau_{pi}} + \frac{1}{2}\frac{x^2_{6i}}{\tau_{qi}} \\ &\quad \left. + \frac{1}{2}\frac{x^2_{7i}}{L_{vi}} + \frac{1}{2}\frac{x^2_{8i}}{L_{vi}}\right] \end{aligned} \quad (24)$$

$$K(x) = \frac{\partial H_a(x_i)}{\partial x_i} = \left[-\frac{1}{L_{fi}}x_{1i}^*, -\frac{1}{L_{fi}}x_{2i}^*, -\frac{1}{C_{fi}}x_{3i}^*, -\frac{1}{C_{fi}}x_{4i}^*, -\frac{1}{\tau_{pi}}x_{5i}^*, -\frac{1}{\tau_{qi}}x_{6i}^*, -\frac{1}{L_{vi}}x_{7i}^*, -\frac{1}{L_{vi}}x_{8i}^*\right]^{\mathrm{T}} \quad (25)$$

where $K(x) = [K_1, K_2, K_3, K_4, K_5, K_6, K_7, K_8]^{\mathrm{T}}$

$$\frac{\partial K_1(x_i)}{\partial x_{ij}} = 0; \quad \frac{\partial K_2(x_i)}{\partial x_{ij}} = 0; \frac{\partial K_3(x_i)}{\partial x_{ij}} = 0; \frac{\partial K_4(x_i)}{\partial x_{ij}} = 0$$
$$\frac{\partial K_5(x_i)}{\partial x_{ij}} = 0; \quad \frac{\partial K_6(x_i)}{\partial x_{ij}} = 0; \frac{\partial K_7(x_i)}{\partial x_{ij}} = 0; \frac{\partial K_8(x_i)}{\partial x_{ij}} = 0 \quad (26)$$

where $j = \{1, \ldots, 8\}$.

This proves that the second condition of integrability $\nabla K_i(x_i) = [\nabla K_i(x_i)]^{\mathrm{T}}$ is verified.

2) Equilibrium Assignment: Using (25) and considering the equilibrium point $x_i^* = (x_{1i}^*, x_{2i}^*, x_{3i}^*, x_{4i}^*, x_{5i}^*, x_{6i}^*, x_{7i}^*, x_{8i}^*)$, the following expression (27) is obtained:

$$K\left(x_i^*\right) = \frac{\partial H_a\left(x_i^*\right)}{\partial x_i} = \left[-\frac{1}{L_{fi}}x_{1i}^*, -\frac{1}{L_{fi}}x_{2i}^*, -\frac{1}{C_{fi}}x_{3i}^*, -\frac{1}{C_{fi}}x_{4i}^*, -\frac{1}{\tau_{pi}}x_{5i}^*, -\frac{1}{\tau_{qi}}x_{6i}^*, -\frac{1}{L_{vi}}x_{7i}^*, -\frac{1}{L_{vi}}x_{8i}^*\right]. \quad (27)$$

From another side

$$-\nabla H\left(x_i^*\right) = \left[-\frac{1}{L_{fi}}x_{1i}^*, -\frac{1}{L_{fi}}x_{2i}^*, -\frac{1}{C_{fi}}x_{3i}^*, -\frac{1}{C_{fi}}x_{4i}^* -\frac{1}{\tau_{pi}}x_{5i}^*, -\frac{1}{\tau_{qi}}x_{6i}^*, -\frac{1}{L_{vi}}x_{7i}^*, -\frac{1}{L_{vi}}x_{8i}^*\right]. \quad (28)$$

From (27) and (28), it can be noted that the equilibrium condition 3 is well verified.

3) Lyapunov Stability:

$$K\left(x_i^*\right) = \left[-\frac{1}{L_{fi}}x_{1i}^*, -\frac{1}{L_{fi}}x_{2i}^*, -\frac{1}{C_{fi}}x_{3i}^*, -\frac{1}{C_{fi}}x_{4i}^* -\frac{1}{\tau_{pi}}x_{5i}^*, -\frac{1}{\tau_{qi}}x_{6i}^*, -\frac{1}{L_{vi}}x_{7i}^*, -\frac{1}{L_{vi}}x_{8i}^*\right] = [0, 0, 0, 0, 0, 0, 0, 0] \quad (29)$$

$$-\nabla_{x_i}^2 H_d\left(x_i^*\right) = -\frac{\partial^2 H_d\left(x_i^*\right)}{\partial x_i^2} = -\left[\frac{2}{L_{fi}} + \frac{2}{C_{fi}} + \frac{1}{\tau_{pi}} + \frac{1}{\tau_{qi}} + \frac{2}{L_{vi}}\right] < 0 \quad (30)$$

where $L_{fi}, C_{fi}, \tau_{pi}, \tau_{qi}$, and L_{vi} are positive coefficients.

4) Invariance of the Equilibrium Point: The fifth condition is to verify the invariance of the equilibrium point using Lasalle's theorem

$$-[\nabla H_d(x_i)]^{\mathrm{T}}\mathcal{R}_d(x_i)\nabla H_d(x_i) = \begin{bmatrix} -\frac{a_{11i}}{L_{fi}}\left(x_{1i} - x_{1i}^*\right)^2 \\ -\frac{a_{22i}}{L_{fi}}\left(x_{2i} - x_{2i}^*\right)^2 \\ -\frac{a_{33i}}{C_{fi}}\left(x_{3i} - x_{i3i}^*\right)^2 \\ -\frac{a_{44i}}{C_{fi}}\left(x_{4i} - x_{4i}^*\right)^2 \\ -\frac{a_{55i}}{\tau_{pi}}\left(x_{5i} - x_{5i}^*\right)^2 \\ -\frac{a_{66i}}{\tau_{qi}}\left(x_{6i} - x_{6i}^*\right)^2 \\ -\frac{a_{77i}}{L_{vi}}\left(x_{7i} - x_{7i}^*\right)^2 \\ -\frac{a_{77i}}{L_{vi}}\left(x_{8i} - x_{8i}^*\right)^2 \end{bmatrix} \leq \quad (31)$$

where $a_{ppi} \geq 0$. This further proves that the equilibrium point is an invariant point and the chosen $H_{di}(x)$ ensures that the solution is bounded.

To better show the stability of the system, eigenvalues of the system have been studied in what follows. For that, the whole microgrid system is modeled. This small-signal model corresponds to the linearization of the system model around its operating point obtained by calculating its Jacobian matrix. This technique presented in [41] is mathematically formulated by building a single model: the DGs and their controls, the interconnections between DGs, and the supplied used local load.

The small-signal model of the studied MG is presented using the following state-space model:

$$\left[\Delta \dot{x}_{mg}\right] = A_{mg}\left[\Delta x_{mg}\right] \quad (32)$$

where A_{mg} represents the global matrix of all the MG in small signal and Δx_{mg} represents their corresponding state variables.

By solving (33), the eigenvalues of the studied MG can be obtained. These values represent the solution of the characteristic equation that characterizes which is related to the different frequencies and damping existing in the studied system allowing to prove and study the stability of the system

$$\det\left(A_{mg} - \lambda I\right) = 0. \quad (33)$$

The resulting eigenvalue spectrum of the studied system is presented in Fig. 5. It can be seen that the obtained eigenvalues are depending on the frequency of the system. Indeed, the high-frequency ones corresponding to the eigenvalues presented in cluster "III" are sensitive to the state variables of *LCL* filter block of the used inverters and its corresponding line currents. The eigenvalues in cluster "II" are largely sensitive to the state variables of the output filter, voltage controller, and current controller. The low-frequency dominant relative to the eigenvalues regrouped in cluster "I" is largely sensitive to the state variables of the power-sharing controller. This obtained result illustrates that by using the proposed control, the obtained eigenvalues of the closed-loop system are characterized by negative real parts, which proves that the proposed control ensures the closed-loop stability

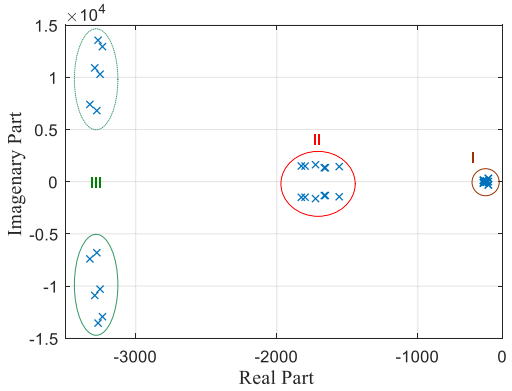

Fig. 5. Complete eigenvalues of the studied microgrid systems.

of the system. Moreover, it can be seen that applied to the studied system, the proposed control guarantees a large stability margin with good decoupling between the eigenvalues allowing to better guarantee the stability of the system.

IV. Comparative Controller

To evaluate the performance of the proposed controller, a comparison test with the DTS droop control is performed [19]. In this technique, the voltage regulation loop is composed of two nested loops based on the conventional PI controller.

The control laws of the inner and the outer loop are expressed on the following expression:

$$\begin{aligned} i_d^* &= G_V(s)\left(v_{Cd} - v_{Cd}^*\right) + i_{Ld} - C_f\omega v_{Cq} \\ i_q^* &= G_V(s)\left(v_{Cq} - v_{Cq}^*\right) + i_{Lq} + C_f\omega v_{Cd} \\ v_d^* &= G_C(s)\left(i_d^* - i_d\right) + R_f i_d - L_f\omega i_q + v_{Cd} \\ v_q^* &= G_C(s)\left(i_q^* - i_q\right) + R_f i_q + L_f\omega i_d + v_{Cq} \end{aligned} \tag{34}$$

where $G_V(s) = k_{pV} + (k_{iV}/s)$ and $G_C(s) = k_{pC} + (k_{iC}/s)$ present, respectively, the PI transfer functions of the outer and inner loops. The decoupled trigonometric droop control laws are expressed as follows:

$$\begin{aligned} \begin{bmatrix} f \\ E \end{bmatrix} = &\begin{bmatrix} \frac{2\delta_f}{\pi} & -\frac{2\delta_f}{\pi} \\ \frac{2\delta_E}{\pi} & \frac{2\delta_E}{\pi} \end{bmatrix} \begin{bmatrix} (\arctan(\mu_p(P^* - P))) \\ (\arctan(\mu_q(Q^* - Q))) \end{bmatrix} \\ &+ \begin{bmatrix} \Delta f \\ \Delta E \end{bmatrix}_{\max} + \begin{bmatrix} \Delta f \\ \Delta E \end{bmatrix}_{\min} + \begin{bmatrix} f^* \\ E^* \end{bmatrix} \end{aligned} \tag{35}$$

with

$$\begin{bmatrix} \Delta f \\ \Delta E \end{bmatrix}_{\max} = \begin{bmatrix} \dfrac{\mathrm{Kpf}_{\max} + \mathrm{KIf}_{\max}}{s} \\ \dfrac{\mathrm{KpV}_{\max} + \mathrm{KIV}_{\max}}{s} \end{bmatrix} \begin{bmatrix} P_{\max} & P \\ Q_{\max} & Q \end{bmatrix} \tag{36}$$

and

$$\begin{bmatrix} \Delta f \\ \Delta E \end{bmatrix}_{\min} = \begin{bmatrix} \dfrac{\mathrm{Kpf}_{\min} + \mathrm{KIf}_{\min}}{s} \\ \dfrac{\mathrm{KpV}_{\min} + \mathrm{KIV}_{\min}}{s} \end{bmatrix} \begin{bmatrix} P_{\min} & P \\ Q_{\min} & Q \end{bmatrix} \tag{37}$$

where E and f are, respectively, the operating voltage and frequency of the inverter, f^* and E^* are, respectively, the frequency and voltage references, δ_f and δ_E denote the coefficients that fix the variation limits of voltage and frequency of the trigonometric function, respectively, and μ_p and μ_q are the control coefficients that set the concavity of the trigonometric function, respectively.

$\mathrm{Kpf}_{\max}$ and $\mathrm{KIf}_{\max}$ are, respectively, the proportional and the integral coefficient related to the frequency and voltage of virtual power sag limit control [19].

The parameters of the inner and the outer loop of the compared control technique are calculated by applying the pole placement technique. ($k_{pV} = 2\xi C_f\omega_V, k_{iV} = C_f\omega_V^2$) and ($k_{pC} = 2\xi L_f\omega_C, k_{iC} = L_f\omega_C^2$), where ξ_V and ω_V are the desired damping factor and bandwidth of the voltage loop and ξ_C and ω_C are separately the desired damping factor and bandwidth of the current loop, respectively. In order to escape the interaction issues between the two loops, the damping factor ξ is set equal to 0.7. whereas the bandwidth of the current loop (ω_C) is set to 2000 rad/s, ten times higher than that of the voltage loop (ω_V).

V. Comparative Experimental Results

The effectiveness of the proposed control structure is verified on a lab-scale MG constituted of three DGs controlled by using a dSPACE 1007 rapid prototyping. The experimental test bench is shown in Fig. 6. The performances of the proposed modular IDA-PBC-E2D control strategy are verified using extensive comparisons with the PI-DTS control strategy detailed in Section IV. The corresponding control and circuit parameters are listed in the Appendix.

A. RL Load

A thorough comparative study has been conducted in the lab-scale MG, shown in Fig. 6, in order to evaluate the performances of the proposed IDA-PBC-E2D compared to the PI-DTS in terms of power-sharing performances and control flexibility. The resulting active and reactive power participation of each DG and its corresponding current waveforms is shown, respectively, in Figs. 8 and 9. In this test, the performances of the proposed IDA-PBC-E2D are evaluated and compared to the PI-DTS when the MG is supplying a resistive inductive linear load of 3.2 kW and 2.2 kVAr as it is shown in Fig. 7. The experimental test has been conducted in three main steps where, in each step, an additional DG unit is connected to test the control performances of the compared methods and their efficacy in maintaining stable performances and accurate power sharing between DGs. The *RL* test considers the following scenario.

1) *From $t = 0$ to $t = 4s$:* Only DG1 supplies the *RL* load
2) *From $t = 4$ to 12 s*: Both DG1 and DG2 supply the *RL* load.
3) *From $t = 12$ to 20 s* : DG1, DG2, and DG3 supply the *RL* load.

As it can be appreciated from Fig. 8, the proposed IDA-PBC-E2D method shows almost similar power-sharing performances compared to the PI-DTS method. However, the PI-DTS method presents considerable power oscillations compared to the proposed method. These oscillations increase when interconnecting more DG units.

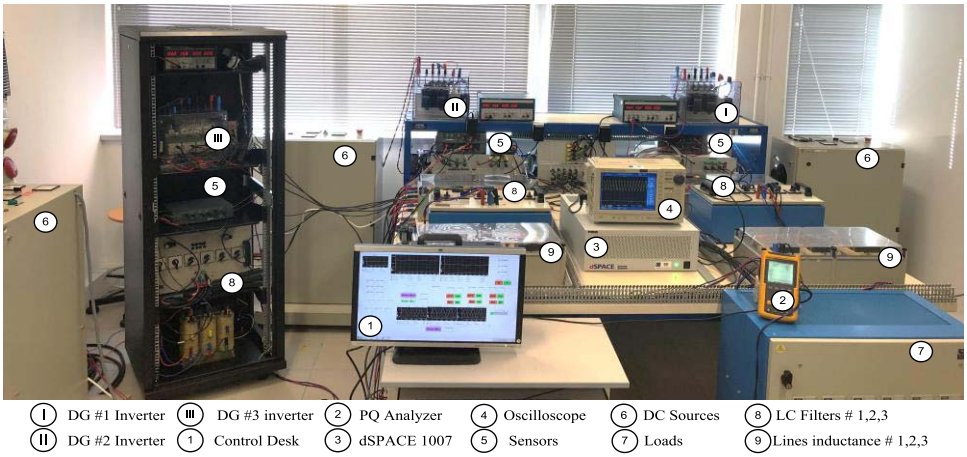

Fig. 6. Experimental test bench of the studied system.

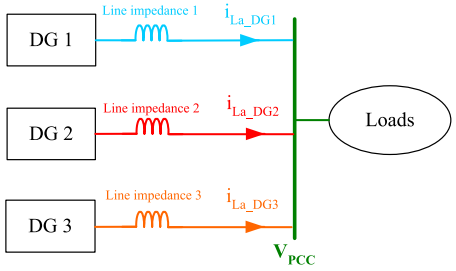

Fig. 7. Configuration of the proposed experimental test.

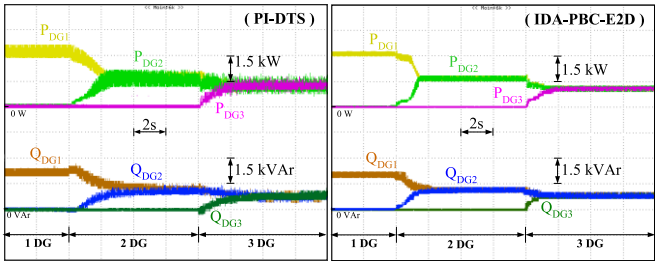

Fig. 8. Experimental comparison between the proposed IDA-PBC-E2D controller (bottom) and the PI-DTS controller before (top) and after (middle) resetting: DG#1, DG#2, and DG#3 active and reactive power sharing for the *RL* load scenario.

The output current waveforms illustrated in Fig. 9 show that the proposed IDA-PBC-E2D method achieves accurate current sharing compared to the PI-DTS method that presents some current-sharing inaccuracy that can introduce circulating currents.

The measured THD rates are summarized in Table I for the different test steps. The proposed IDA-PBC-E2D method ensures satisfactory harmonic performances by maintaining the total voltage harmonic distortions in small rate around 0.62% independently of the MG configuration. This is not the case when applying the PI-DTS controller, which presents a high THD rates with large variations that go from 1.2% to 1.52% depending on the number of the used DG. The obtained results demonstrate the superiority of the proposed IDA-PBC-E2D in maintaining stable performances and accurate power sharing compared to the PI-DTS control that shows some weakness to accommodate MG expansion as it needs to be

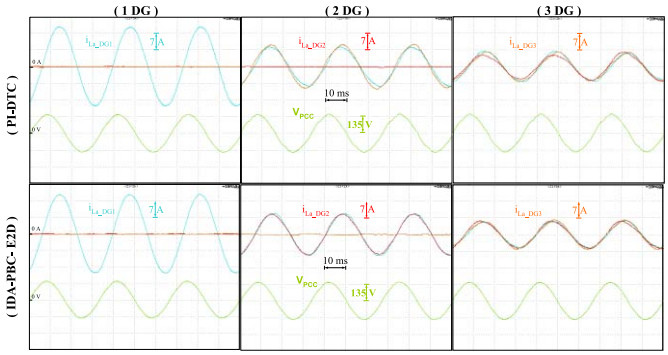

Fig. 9. Experimental comparison between the proposed IDA-PBC-E2D controller (bottom) and the PI-DTS controller before (top) and after (middle) resetting: DG#1, DG#2, and DG#3 active and reactive power sharing for the *RL* load scenario.

TABLE I
VOLTAGE THD RATES—RL LOAD

THDv	**1 DG**	**2 DG**	**3 DG**
PI-DTS	1.2%	1.24%	1.52%
IDA-PBC-E2D	**0.63%**	**0.64%**	**0.65%**

adapted for each configuration. On the other side, the proposed IDA-PBC-E2D achieves accurate power sharing with fewer oscillations even when interconnecting multiple DG units. This confirms the modular functionality of the proposed IDA-PBC-E2D technique that can be designed to include multiple DGs, which is of importance to preserve the scalability of MGs.

B. Nonlinear Load

In this section, the effectiveness of the proposed IDA-PBC-E2D control strategy is verified when the MG is supplying the nonlinear load shown in Fig. 10. This load consists of a three-phase diode rectifier with 20% of current harmonics.

The test consists of the following scenario.

1) *From $t = 0$ to $t = 2$ s (Z1):* Only DG1 supplies the load (3.3 kW and 300 VAr).
2) *From $t = 2$ to 8 s (Z2):* Both DG1 and DG2 supply the load (3.3 kW and 300 VAr).

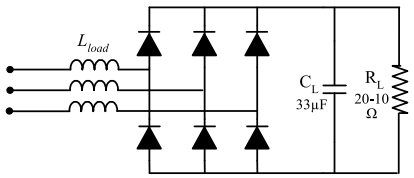

Fig. 10. Nonlinear load.

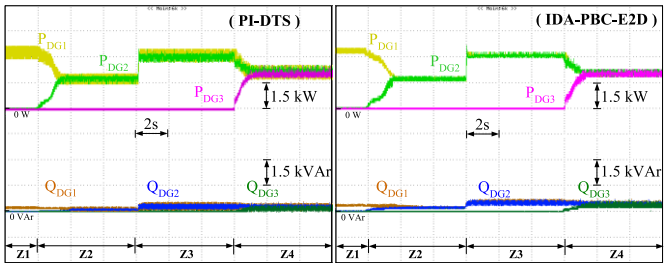

Fig. 11. Experimental comparison between the proposed IDA-PBC-E2D controller (right) and the PI-DTS controller (left): DG#1, DG#2, and DG#3 active and reactive power sharing for the nonlinear load.

3) *From $t = 8$ to 14 s (Z3):* Only DG1 and DG2 supply the load that increases from (3.3 kW and 300 VAr) to (6 kW and 600 VAr).
4) *From $t = 14$ to 20 s (Z4):* DG1, DG2, and DG3 supply the load (6 kW and 600 VAr).

The obtained active and reactive powers are shown in Fig. 11 to compare between the proposed IDA-PBC-E2D control technique and the PI-DTS. It can be noted that when supplying the nonlinear load, both control techniques show similar active and reactive power-sharing performances. However, the proposed IDA-PBC-E2D offers higher performances characterized by lower oscillations than the PI-DTS under nonlinear load changes either when two or three DGs are connected.

The obtained results confirm the advantages of the proposed control in maintaining the system stability even under MG expansion. The proposed control achieves stable and modular control independently of the MG architecture, i.e., the number of interconnected DG units and loads.

Moreover, Fig. 12 shows the waveforms of the PCC voltage and the output current of each DG unit phase "a." It can be appreciated from this figure that the proposed control strategy allows maintaining accurate load current sharing between the interconnected DGs. By following the obtained voltage, THD rates are summarized in Table II. It can be seen that the proposed IDA-PBC-E2D allows obtaining better performances than the PI-DTS, which can be noticed when comparing the measured voltage THD rates. Indeed, the superiority of the proposed method is highlighted as it obtained smaller THD rates between 3.14% and 3.58% than the PI-DTS that obtained values between 4.17% and 5.91%. Note that the maximum allowable voltage THD value is fixed to 5% by the IEEE 1547-2018 Standard [42].

Following the two experiment tests, it can be concluded that the proposed IDA-PBC-E2D control ensures better power quality and more accurate power-sharing performances than

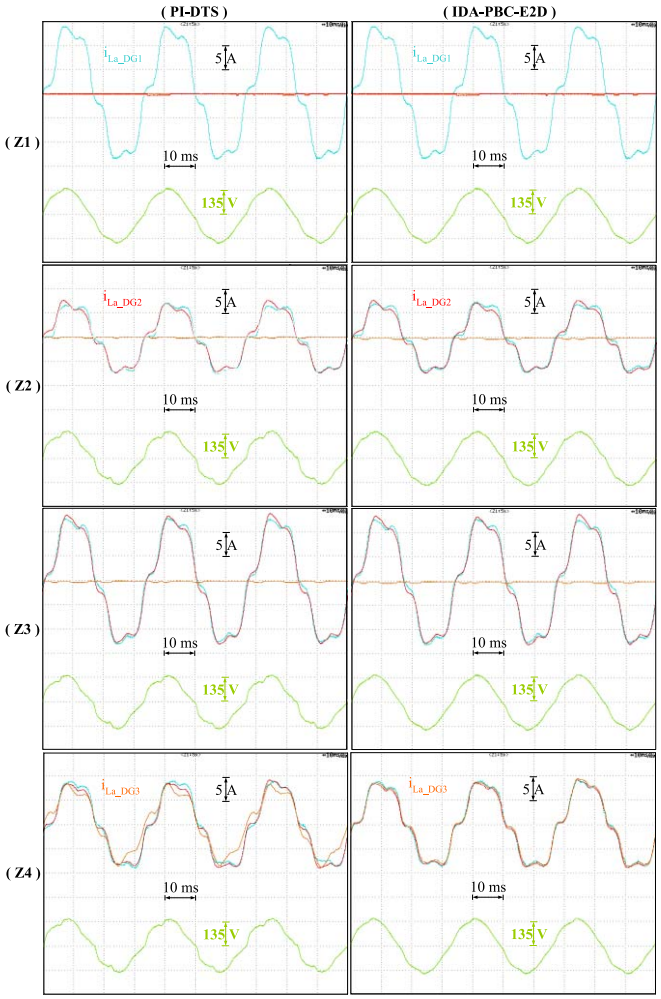

Fig. 12. Experimental comparison between the proposed IDA-PBC-E2D controller (right) and the PI-DTS controller (left): DG#1, DG#2, and DG#3 output currents (Phase-a), and the PCC voltage under a nonlinear load when one DG (Z1), two DGs (Z2), additional nonlinear step load (Z3), and three DGs (Z4) are supplying the system.

TABLE II
VOLTAGE THD RATES—NONLINEAR LOAD

THDv	PI-DTS	IDA-PBC-E2D
Z1	4.17%	**3.14%**
Z2	4.97%	**3.31%**
Z3	5.85%	**3.36%**
Z3	5.91%	**3.58%**

the PI-DTS. Moreover, it is shown that the proposed method allows maintaining stable performances even when additional DGs and loads are connected to the MG, which confirms the modular functionality that characterizes the proposed control technique. Indeed, the design methodology of the proposed control strategy guarantees the stability of the system as well as its modularity even under system reconfiguration and expansion, which sustains the plug and play characteristic in MGs.

VI. CONCLUSION

This article has proposed a modular control strategy based on passivity to guarantee proper voltage control and accurate

power sharing in islanded MGs with multiple DG units. This control is based on an interesting modeling formalism called the "PCH" that permits not only to synthesize a stable control but also to extend the study to a system with several DG units due to the modularity of the used energetic model. The system modeling in the Hamiltonian form and the controller synthetizer are comprehensively detailed. Extensive comparisons between the proposed E2D control using the IDA-PBC and an advanced control technique based on a decoupled droop control are presented. The carried experimental tests show that the proposed approach ensures satisfactory voltage quality and accurate active and reactive power sharing even under system expansion, which confirms the modular functionality of the proposed control technique.

APPENDIX

System Parameters: $L_{fi} = 3$ mH, $r_{fi} = 0.1\ \Omega$, $C_{fi} = 44\ \mu$F, $L_{L1} = 1$ mH, $L_{L2} = 2$ mH, $U_{DCi} = 450$ V, $F_s = 10$ kHz, and Rated voltage : 110 Vrms, 60 Hz.

Control Parameters: $a_{11i} = a_{22i} = 1, a_{33i} = a_{44i} = 1, a_{13i} = -a_{31i} = 1, a_{24i} = -a_{42i} = 1, a_{55i} = a_{66i} = 0, a_{77i} = a_{88i} = 0, k_{pV} = 0.024, k_{iV} = 2.82, a_{37i} = -a_{73i} = 0,, a_{48i} = -a_{84i} = 0, \lambda_i = 8, \xi_i = -8, Kpi = Kqi = 1e{-}5, k_{iC} = 16922,$ and $k_{pC} = 14.15$.

REFERENCES

[1] V. Krishnamurthy and A. Kwasinski, "Effects of power electronics, energy storage, power distribution architecture, and lifeline dependencies on microgrid resiliency during extreme events," *IEEE J. Emerg. Sel. Topics Power Electron.*, vol. 4, no. 4, pp. 1310–1323, Dec. 2016, doi: 10.1109/JESTPE.2016.2598648.

[2] N. Khefifi, A. Houari, Mohamed. Machmoum, and M. Ghanes, "Interconnection and damping assignment passivity for the control of PV/battery hybrid power source in islanded microgrid," *Int. J. Renew. Energy Res. (IJRER)*, vol. 9, no. 4, pp. 1790–1802, Dec. 2019.

[3] V. Mohan, R. Suresh, J. G. Singh, W. Ongsakul, and N. Madhu, "Microgrid energy management combining sensitivities, interval and probabilistic uncertainties of renewable generation and loads," *IEEE J. Emerg. Sel. Topics Circuits Syst.*, vol. 7, no. 2, pp. 262–270, Jun. 2017, doi: 10.1109/JETCAS.2017.2679030.

[4] F. Zandi, B. Fani, I. Sadeghkhani, and A. Orakzadeh, "Adaptive complex virtual impedance control scheme for accurate reactive power sharing of inverter interfaced autonomous microgrids," *IET Gener., Transmiss. Distrib.*, vol. 12, no. 22, pp. 6021–6032, Dec. 2018, doi: 10.1049/iet-gtd.2018.5123.

[5] Z. Wang, W. Wu, and B. Zhang, "A distributed quasi-Newton method for droop-free primary frequency control in autonomous microgrids," *IEEE Trans. Smart Grid*, vol. 9, no. 3, pp. 2214–2223, May 2018, doi: 10.1109/TSG.2016.2609422.

[6] R. Bhattarai, N. Gurung, and S. Kamalasadan, "Dual mode control of a three-phase inverter using minimum variance adaptive architecture," *IEEE Trans. Ind. Appl.*, vol. 54, no. 4, pp. 3868–3880, Jul. 2018, doi: 10.1109/TIA.2018.2826469.

[7] Y. Kwon, A. Kwasinski, and A. Kwasinski, "Coordinated energy management in resilient microgrids for wireless communication networks," *IEEE J. Emerg. Sel. Topics Power Electron.*, vol. 4, no. 4, pp. 1158–1173, Dec. 2016, doi: 10.1109/JESTPE.2016.2614425.

[8] X. Hou, Y. Sun, H. Han, Z. Liu, W. Yuan, and M. Su, "A fully decentralized control of grid-connected cascaded inverters," *IEEE Trans. Sustain. Energy*, vol. 10, no. 1, pp. 315–317, Jan. 2019, doi: 10.1109/TPWRD.2018.2816813.

[9] H. Han, X. Hou, J. Yang, J. Wu, M. Su, and J. M. Guerrero, "Review of power sharing control strategies for islanding operation of AC microgrids," *IEEE Trans. Smart Grid*, vol. 7, no. 1, pp. 200–215, Jan. 2016, doi: 10.1109/TSG.2015.2434849.

[10] Y. Du, X. Lu, J. Wang, B. Chen, H. Tu, and S. Lukic, "Dynamic microgrids in resilient distribution systems with reconfigurable cyber-physical networks," *IEEE J. Emerg. Sel. Topics Power Electron.*, early access, Mar. 19, 2020, doi: 10.1109/JESTPE.2020.2981921.

[11] P. Zhang, H. Zhao, H. Cai, J. Shi, and X. He, "Power decoupling strategy based on 'virtual negative resistor'for inverters in low-voltage microgrids," *IET Power Electron.*, vol. 9, no. 5, pp. 1037–1044, 2016, doi: 10.1049/iet-pel.2015.0137.

[12] U. B. Tayab, M. A. B. Roslan, L. J. Hwai, and M. Kashif, "A review of droop control techniques for microgrid," *Renew. Sustain. Energy Rev.*, vol. 76, pp. 717–727, Sep. 2017, doi: 10.1016/j.rser.2017.03.028.

[13] B. K. Unnikrishnan, M. S. Johnson, and E. P. Cheriyan, "Small signal stability improvement of a microgrid by the optimised dynamic droop control method," *IET Renew. Power Gener.*, vol. 14, no. 5, pp. 822–833, Apr. 2020, doi: 10.1049/iet-rpg.2019.0428.

[14] Z. Peng *et al.*, "Droop control strategy incorporating coupling compensation and virtual impedance for microgrid application," *IEEE Trans. Energy Convers.*, vol. 34, no. 1, pp. 277–291, Mar. 2019, doi: 10.1109/TEC.2019.2892621.

[15] A. Saim, A. Houari, M. A. Ahmed, A. Djerioui, M. Machmoum, and J. M. Guerrero, "Adaptive reference trajectory for power quality enhancement in three-phase four-wire standalone power supply systems with nonlinear and unbalanced loads," *IEEE J. Emerg. Sel. Topics Power Electron.*, vol. 8, no. 2, pp. 1593–1603, Jun. 2020, doi: 10.1109/JESTPE.2020.2966923.

[16] A. Haddadi, A. Yazdani, G. Joos, and B. Boulet, "A gain-scheduled decoupling control strategy for enhanced transient performance and stability of an islanded active distribution network," *IEEE Trans. Power Del.*, vol. 29, no. 2, pp. 560–569, Apr. 2014, doi: 10.1109/TPWRD.2013.2278376.

[17] Y. Xu, Q. Guo, H. Sun, and Z. Fei, "Distributed discrete robust secondary cooperative control for islanded microgrids," *IEEE Trans. Smart Grid*, vol. 10, no. 4, pp. 3620–3629, Jul. 2019, doi: 10.1109/TSG.2018.2833100.

[18] T. Wu, Z. Liu, J. Liu, S. Wang, and Z. You, "A unified virtual power decoupling method for droop-controlled parallel inverters in microgrids," *IEEE Trans. Power Electron.*, vol. 31, no. 8, pp. 5587–5603, Aug. 2016, doi: 10.1109/TPEL.2015.2497972.

[19] A. E. M. Bouzid, P. Sicard, H. Chaoui, A. Cheriti, M. Sechilariu, and J. M. Guerrero, "A novel decoupled trigonometric saturated droop controller for power sharing in islanded low-voltage microgrids," *Electr. Power Syst. Res.*, vol. 168, pp. 146–161, Mar. 2019, doi: 10.1016/j.epsr.2018.11.016.

[20] J. Lai, X. Lu, X. Yu, and A. Monti, "Stochastic distributed secondary control for AC microgrids via event-triggered communication," *IEEE Trans. Smart Grid*, vol. 11, no. 4, pp. 2746–2759, Jul. 2020, doi: 10.1109/TSG.2020.2966691.

[21] H. R. Baghaee, M. Mirsalim, G. B. Gharehpetan, and H. A. Talebi, "Nonlinear load sharing and voltage compensation of microgrids based on harmonic power-flow calculations using radial basis function neural networks," *IEEE Syst. J.*, vol. 12, no. 3, pp. 2749–2759, Sep. 2018, doi: 10.1109/JSYST.2016.2645165.

[22] H. R. Baghaee, M. Mirsalim, and G. B. Gharehpetian, "Power calculation using RBF neural networks to improve power sharing of hierarchical control scheme in multi-DER microgrids," *IEEE J. Emerg. Sel. Topics Power Electron.*, vol. 4, no. 4, pp. 1217–1225, Dec. 2016, doi: 10.1109/JESTPE.2016.2581762.

[23] M. Hamzeh, S. Emamian, H. Karimi, and J. Mahseredjian, "Robust control of an islanded microgrid under unbalanced and nonlinear load conditions," *IEEE J. Emerg. Sel. Topics Power Electron.*, vol. 4, no. 2, pp. 512–520, Jun. 2016, doi: 10.1109/JESTPE.2015.2459074.

[24] M. Pichan and H. Rastegar, "Sliding-mode control of four-leg inverter with fixed switching frequency for uninterruptible power supply applications," *IEEE Trans. Ind. Electron.*, vol. 64, no. 8, pp. 6805–6814, Aug. 2017, doi: 10.1109/TIE.2017.2686346.

[25] M. Shahparasti, M. Mohamadian, A. Yazdian, A. A. Ahmad, and M. Amini, "Derivation of a stationary-frame single-loop controller for three-phase standalone inverter supplying nonlinear loads," *IEEE Trans. Power Electron.*, vol. 29, no. 9, pp. 5063–5071, Sep. 2014, doi: 10.1109/TPEL.2013.2287906.

[26] S. J. Williamson, A. Griffo, B. H. Stark, and J. D. Booker, "A controller for single-phase parallel inverters in a variable-head pico-hydropower off-grid network," *Sustain. Energy, Grids Netw.*, vol. 5, pp. 114–124, Mar. 2016, doi: 10.1016/j.segan.2015.11.006.

[27] Z. Li, C. Zang, P. Zeng, H. Yu, S. Li, and J. Bian, "Control of a grid-forming inverter based on sliding-mode and mixed H_2/H_∞ control," *IEEE Trans. Ind. Electron.*, vol. 64, no. 5, pp. 3862–3872, May 2017, doi: 10.1109/TIE.2016.2636798.

[28] W. Lu, K. Zhou, D. Wang, and M. Cheng, "A general parallel structure repetitive control scheme for multiphase DC–AC PWM converters," *IEEE Trans. Power Electron.*, vol. 28, no. 8, pp. 3980–3987, Aug. 2013, doi: 10.1109/TPEL.2012.2229395.
[29] S. Jiang, D. Cao, Y. Li, J. Liu, and F. Z. Peng, "Low-THD, fast-transient, and cost-effective synchronous-frame repetitive controller for three-phase UPS inverters," *IEEE Trans. Power Electron.*, vol. 27, no. 6, pp. 2994–3005, Jun. 2012, doi: 10.1109/TPEL.2011.2178266.
[30] H. T. Nguyen, E.-K. Kim, I.-P. Kim, H. H. Choi, and J.-W. Jung, "Model predictive control with modulated optimal vector for a three-phase inverter with an LC filter," *IEEE Trans. Power Electron.*, vol. 33, no. 3, pp. 2690–2703, Mar. 2018, doi: 10.1109/TPEL.2017.2694049.
[31] J. Zhang, L. Li, D. G. Dorrell, M. Norambuena, and J. Rodriguez, "Predictive voltage control of direct matrix converters with improved output voltage for renewable distributed generation," *IEEE J. Emerg. Sel. Topics Power Electron.*, vol. 7, no. 1, pp. 296–308, Mar. 2019, doi: 10.1109/JESTPE.2018.2874275.
[32] S. Pang, B. Nahid-Mobarakeh, S. Pierfederici, Y. Huangfu, G. Luo, and F. Gao, "Towards stabilization of constant power loads using IDA-PBC for cascaded LC filter DC/DC converters," *IEEE J. Emerg. Sel. Topics Power Electron.*, early access, Oct. 3, 2019, doi: 10.1109/JESTPE.2019.2945331.
[33] R. Ortega, M. W. Spong, F. Gomez-Estern, and G. Blankenstein, "Stabilization of a class of underactuated mechanical systems via interconnection and damping assignment," *IEEE Trans. Autom. Control*, vol. 47, no. 8, pp. 1218–1233, Aug. 2002, doi: 10.1109/TAC.2002.800770.
[34] S. Sanchez, R. Ortega, R. Grino, G. Bergna, and M. Molinas, "Conditions for existence of equilibria of systems with constant power loads," *IEEE Trans. Circuits Syst. I, Reg. Papers*, vol. 61, no. 7, pp. 2204–2211, Jul. 2014, doi: 10.1109/TCSI.2013.2295953.
[35] N. Khefifi, A. Houari, M. Machmoum, M. Ghanes, and M. Ait-Ahmed, "Control of grid forming inverter based on robust IDA-PBC for power quality enhancement," *Sustain. Energy, Grids Netw.*, vol. 20, Dec. 2019, Art. no. 100276, doi: 10.1016/j.segan.2019.100276.
[36] R. V. Meshram, M. Bhagwat, S. Khade, S. R. Wagh, A. M. Stankovic, and N. M. Singh, "Port-controlled phasor Hamiltonian modeling and IDA-PBC control of solid-state transformer," *IEEE Trans. Control Syst. Technol.*, vol. 27, no. 1, pp. 161–174, Jan. 2019, doi: 10.1109/TCST.2017.2761866.
[37] M. Hilairet, M. Ghanes, O. Béthoux, V. Tanasa, J.-P. Barbot, and D. Normand-Cyrot, "A passivity-based controller for coordination of converters in a fuel cell system," *Control Eng. Pract.*, vol. 21, no. 8, pp. 1097–1109, Aug. 2013, doi: 10.1016/j.conengprac.2013.04.003.
[38] J. M. Guerrero, L. Hang, and J. Uceda, "Control of distributed uninterruptible power supply systems," *IEEE Trans. Ind. Electron.*, vol. 55, no. 8, pp. 2845–2859, Aug. 2008, doi: 10.1109/TIE.2008.924173.
[39] A. Zurfi and J. Zhang, "Investigation of the line frequency for demand-side primary frequency control using behind-the-meter home batteries," *Int. J. Renew. Energy Res. (IJRER)*, vol. 8, no. 2, pp. 784–796, Jun. 2018.
[40] C. Li, S. K. Chaudhary, M. Savaghebi, J. C. Vasquez, and J. M. Guerrero, "Power flow analysis for low-voltage AC and DC microgrids considering droop control and virtual impedance," *IEEE Trans. Smart Grid*, vol. 8, no. 6, pp. 2754–2764, Nov. 2017, doi: 10.1109/TSG.2016.2537402.
[41] N. Pogaku, M. Prodanovic, and T. C. Green, "Modeling, analysis and testing of autonomous operation of an inverter-based microgrid," *IEEE Trans. Power Electron.*, vol. 22, no. 2, pp. 613–625, Mar. 2007, doi: 10.1109/TPEL.2006.890003.
[42] *IEEE Standard for Interconnection and Interoperability of Distributed Energy Resources with Associated Electric Power Systems Interfaces*, IEEE Standard 1547-2018 (Revision of IEEE Standard 1547-2003), Apr. 2018, pp. 1–138, doi: 10.1109/IEEESTD.2018.8332112.

Nidhal Khefifi received the Electrical Engineering degree from the École nationale supérieure d'ingénieurs de Tunis (ENSIT), Tunis, Tunisia, in 2016, and the M.S. degree in information and system sciences from Aix-Marseille Université, Marseille, France, in 2017. He is currently pursuing the Ph.D. degree with a focus on the power quality and stability of microgrids with the Institutde Recherche en Energie Electrique de Nantes Atlantique (IREENA), University of Nantes, Nantes, France.

Azeddine Houari received the Engineering degree in electrical engineering from the University of Bejaia, Béjaïa, Algeria, in 2008, and the Ph.D. degree in electrical engineering from the University of Lorraine, Lorraine, France, in 2012.

Since 2014, he has been an Assistant Professor with the University of Nantes, Saint-Nazaire, France, where he carried out research activities at the Institutde Recherche en Energie Electrique de Nantes Atlantique (IREENA). His current research deals with the power quality and the stability issues in stationary and embedded dc and ac microgrids.

Mohamed Machmoum received the Engineering degree from the Institut Supérieur Industriel, Liège, Belgium, in 1984, and the master's and Ph.D. degrees from the l'Institut National Polytechnique de Lorraine (INPL), Lorraine, France, in 1985 and 1989, respectively, all in electrical engineering.

In 1991, he joined the École Polytechnique de l'Université de Nantes, Nantes, France, as an Assistant Professor, where he has been a Full Professor since September 2005. He is currently the Head of the Institut de Recherche en Energie Electrique de Nantes Atlantique (IREENA), University of Nantes, Saint-Nazaire, France. His main area of interest includes power electronics, power quality, wind and tidal energy conversion systems, and microgrids. In these fields, he has supervised more than 25 Ph.D. students and published one book related to modeling of electrical machines, several chapter books, and nearly 240 journals and conferences in his areas of expertise.

Abdelhakim Saim received the B.S. and M.S. degrees in electronics and control engineering from Blida University, Blida, Algeria, in 2010 and 2012, respectively, and the Ph.D. degree in control engineering from the University of Tizi Ouzou, Tizi Ouzou, Algeria, in 2017.

Since 2017, he has been an Assistant Professor with the Department of Control and Instrumentation, University of Sciences and Technology Houari Boumediene, Algiers, Algeria. He is currently with the Institut de Recherche en Energie Electrique de Nantes Atlantique (IREENA), University of Nantes, Saint-Nazaire, France. His research deals with the power quality and stability of microgrids.

Malek Ghanes received the M.Sc. and Ph.D. degrees in applied automatic and informatics from IRCCyN (now LS2N), Centrale Nantes (CN), Nantes, France, in 2002 and 2005, respectively.

From September 2005 to September 2006, he held a post-doctoral position at GREYC Laboratory. From September 2006 to April 2016, he was with the ECS-Lab, Quartz, ENSEA, Cergy, France, where he was an Associate Professor and the Head of the Department of Automatic and Electrical Engineering. In May 2016, he was promoted as a Full Professor at LS2N-ECN. He has published more than 100 journals articles and conference papers. He holds several patents. His research interests include observation and control of nonlinear systems with applications to electric systems.

Prof. Ghanes was a recipient of the Best Paper Award from the *Control Engineering Practice* (CEP) journal in 2013 and the Applied Research Award from the Federation of Electronic, Electrical and Communications Industries (FIEEC) in 2015. He is currently holding the Chair on Electric Vehicle performances between Renault and CN. He has served as an Associate Editor for the IFAC CEP journal from 2012 to 2020.